AGU PUBLICATIONS

Geophysical Research Letters

RESEARCH LETTER
10.1002/2015GL064670

Key Points:
- Postseismic deformation in Kashmir varies laterally
- Crustal sutures have mechanical implications
- Material heterogeneity can look like blind afterslip

Supporting Information:
- Figures S1–S3

Correspondence to:
R. Bendick,
bendick@mso.umt.edu

Citation:
Bendick, R., S. F. Khan, R. Bürgmann, F. Jouanne, P. Banerjee, M. A. Khan, and R. Bilham (2015), Postseismic relaxation in Kashmir and lateral variations in crustal architecture and materials, *Geophys. Res. Lett.*, *42*, doi:10.1002/2015GL064670.

Received 21 MAY 2015
Accepted 22 MAY 2015
Accepted article online 26 MAY 2015

Postseismic relaxation in Kashmir and lateral variations in crustal architecture and materials

R. Bendick[1], S. F. Khan[2], R. Bürgmann[3], F. Jouanne[4], P. Banerjee[5], M. A. Khan[6], and R. Bilham[7]

[1]Department of Geosciences, University of Montana, Missoula, Montana, USA, [2]NCEG, University of Peshawar, Peshawar, Pakistan, [3]Department of Earth and Planetary Science, University of California, Berkeley, California, USA, [4]ISterre, Université de Savoie, Le Bourget du lac, France, [5]Earth Observatory of Singapore, Nanyang Technological University, Singapore, [6]National Centre for Excellence in Geology, University of Peshawar, Peshawar, Pakistan, [7]CIRES, University of Colorado Boulder, Boulder, Colorado, USA

Abstract Thirty horizontal displacement time series from GPS sites in the area around the 2005 Kashmir earthquake show lateral spatial variations in displacement magnitude and relaxation time for the postseismic interval from 2005 to 2012. The observed spatial pattern of surface displacements can only be reproduced by finite element models of postseismic deformation in elastic over viscoelastic crust that include lateral differences in both the thickness of the elastic layer and the viscosity of the viscoelastic layer. Solutions reproducing the sign of horizontal displacements everywhere in the epicentral region also require afterslip on the portion of the fault dislocation in the viscoelastic layer but not in the elastic lid. Although there are substantial tradeoffs among contributions to postseismic displacements of the surface, the observations preclude both crustal homogeneity and shallow afterslip. In the best family of solutions, the thickness of the elastic upper crust differs by a factor of 5 and the viscosity of the middle and lower crust by an order of magnitude between domains north and south of a suture zone containing the Main Boundary Thrust and Main Mantle Thrust.

1. Introduction

The continental lithosphere responds to instantaneous perturbations to the state of stress (by earthquakes or surface loads) with transient changes to the surface velocity field [*Bürgmann and Dresen*, 2008]. Both the magnitude and characteristic time constants of these velocity transients contain information about the material properties of the crustal architecture that is not accessible from the steady state velocity field [*Flesch and Bendick*, 2012; *Lechmann et al.*, 2011; *Hetland and Hager*, 2004; *Savage*, 2000; *Zatman*, 2000]. Therefore, the best constraints on the presence of lateral rheological heterogeneity in the continental crust and upper mantle arise from the postseismic surface response to a large seismic perturbation.

Postseismic surface displacements following the Wenchuan earthquake in 2008 demonstrate just such sensitivity to lateral variations in crustal architecture and material properties [*Huang et al.*, 2014] between the Tibetan crust and adjacent Sichuan Basin. The lateral crustal heterogeneity in this region was already inferred from differences in the surface strain rate [e.g., *Flesch et al.*, 2005], seismic tomography [*Li et al.*, 2009], and topography [*Wang et al.*, 2012; *Royden et al.*, 2008] requiring at least 2 orders of magnitude of difference in effective lower crustal viscosity across the Longmen Shan in order to persist into the interseismic deformation field. Specifically, postseismic inversions require effective viscosities of 1×10^{17} to 1×10^{18} Pa s for Tibetan crust and $>1\times10^{20}$ Pa s for the Sichuan Block [*Huang et al.*, 2014], confirming that the largest magnitude mechanical differences in the lithosphere influence both postseismic and interseismic deformation but are consistent for both steady state and transient forcing.

Like the Wenchuan event, the 2005 Kashmir earthquake rupture is also embedded in geologically heterogeneous continental lithosphere, with the heterogeneity inferred from the surface expression of structural observations of the Main Boundary Thrust (MBT) and Main Mantle Thrust (MMT) (Figure 1). However, the differences in material parameters are unlikely to be as large as those in Sichuan, because associated lateral variations in interseismic strain rate and topographic slope are much smaller. The lateral difference in mechanical properties is therefore likely to be less than that between Tibet and the Sichuan Basin, and more representative of intraorogen variations, perhaps comparable to or smaller than viscosity contrasts observed across the Kunlun Fault [*Ryder et al.*, 2011]. We simplify the complex

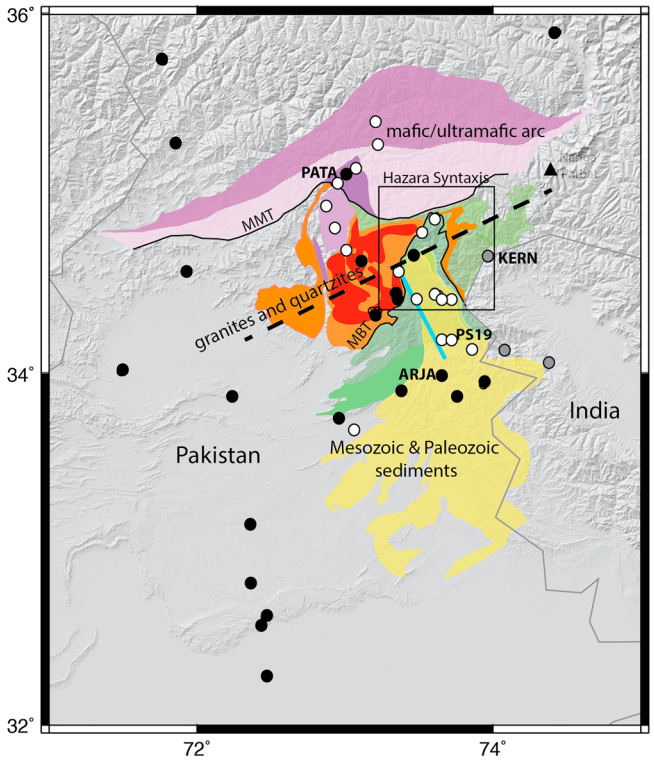

Figure 1. The extended rupture region. GPS sites are marked as circles, solid black were installed by the Universities of Montana and Colorado, white were installed by the University of Savoie, and grey were installed by the Earth Observatory of Singapore. Surface geology is modified from *Searle and Khan* [1996] to emphasize crystalline versus sedimentary units. The Hazara Syntaxis region is outlined with a square and the approximate surface rupture with a cyan line. The approximation of the primary mechanical discontinuity in the numerical simulations is shown by the dashed black line.

structures in the Kashmir region in the form of a discontinuity in physical properties from SE to NW at the NW end of the 2005 rupture.

Coseismic slip models for the rupture inverted from seismic waveforms [*Parsons et al.*, 2006], optical image correlation [*Avouac et al.*, 2006], GPS [*Bendick et al.*, 2007], and SAR interferometry [*Yan et al.*, 2013; *Pathier et al.*, 2006] all indicate 4–8 m of slip on a ~30° dipping plane reaching the surface along a 75 km long rupture trace on the Tanda and Muzaffarabad faults (Figure 1). Some data have been interpreted to support a second fault segment with much less slip to the north [*Bendick et al.*, 2007] or northeast [*Jouanne et al.*, 2011] of the main rupture, based on relatively large coseismic [*Bendick et al.*, 2007] or postseismic [*Jouanne et al.*, 2011] surface displacements north of the termination of the main rupture.

This northern end of the main rupture approaches both the Himalayan Main Boundary Thrust and the Main Mantle Thrust, two primary crustal sutures very near one another in the Hazara Syntaxis (Figure 1). These two major structural discontinuities separate Mesozoic and younger sedimentary rocks in the south from Cambrian-Ordovician granites and Proterozoic quartzite, then adjacent mafic and ultramafic igneous and amphibolite grade metamorphic rocks of the Kohistan arc north of the suture [*Searle and Khan*, 1996]. Therefore, the region hosting the instantaneous stress perturbation from the Kashmir earthquake contains a sharp lithologic contrast between sedimentary rocks on Indian Craton to the south and crystalline rocks of the Tethyan margin to the north. There are few available additional geophysical constraints, such as heat flow or seismic velocity, on the likely material properties of crustal terranes in the region, although detailed studies have been made of the immediate Nanga Parbat area indicating high heat flow and a very shallow brittle-ductile transition [e.g., *Meltzer et al.*, 2001].

2. Methods

We observed surface displacements at 19 locations in Pakistan and India over the time interval 2005–2010 using campaign and semicontinuous geodetic GPS (Figure 1). We also processed raw observations from 18 sites previously described in *Jouanne et al.* [2011] and three additional sites in India. Not all sites were observed at all measurement epochs, and the total amount of data at each site varies considerably (Figure S3 in the supporting information). Sites were divided into regions based on their arrangement relative to the structural discontinuities and the rupture dislocation. We classify 9 sites located more than 100 km from the epicenter as "far field," 9 sites are in the epicentral region in crystalline units north of the Kohistan suture, and 22 sites are in the epicentral region and in sedimentary units south of the suture (Figure 1).

All raw observations were processed for daily positions using GAMIT, MIT's geodetic GPS processing software. These daily positions are then combined into multiday averages. The multiday average positions are used

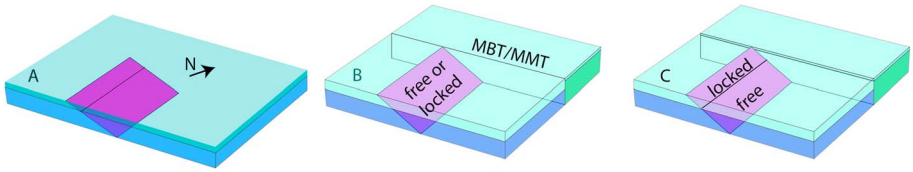

Figure 2. The numerical simulations consist of finite element solutions for time-dependent displacements after coseismic slip on a finite dislocation (pink plane). Families of simulations include those with (a) laterally homogeneous elastic lids over viscoelastic layers, (b) lateral variations in lid thickness and underlying viscosity, and (c) locked or free domains on the fault plane.

directly in the displacement time series for comparison with simulated time series from a range of numerical solutions for the postseismic displacement. To reduce the observed displacement time series, we first estimate an interseismic linear secular velocity for all sites by fitting a linear function with a total of 14 mm/yr of shortening over 520 km between the far-field sites in the Salt Range and western Pakistan and through those in Ladakh, hence spanning the epicentral region. Such a simple interpolation is justified by the observed velocity gradients in GPS measurements of interseismic deformation near the epicentral region [*Jouanne et al*., 2011; *Kundu et al*., 2014; *Schiffman et al*., 2013; *Jouanne et al*., 2011; *Khan et al*., 2008]. We then subtract displacement due to this estimated interseismic velocity from the displacement time series for all epicentral sites (within 100 km of the rupture). We confirm that this estimate removes the secular tectonic velocity from the time series by initially fitting linear + logarithmic functions to each displacement time series; the coefficient of the linear term in all cases is at least 2 orders of magnitude less than the weight of the logarithmic term. The residual displacement of each site for each observation epoch forms the postseismic displacement time series for each site in the epicentral region for comparison to simulations. Next, we fit a logarithmic function (without a linear term) to each reduced time series of form $y = A1n\left\{1+\frac{t}{\tau}\right\}$, where A is the displacement amplitude and τ is the relaxation time constant, both allowed to vary in fitting. Because all of these sites are campaign measurements, we do not estimate periodic terms. We use this function to estimate horizontal postseismic displacements at each GPS site for an epoch after 7 years, so that we can compare the displacements from sites with very different observation durations.

We use the finite element software COMSOL to forward model the expected surface displacements for four different families of rheological architecture (each with a range of material properties) (Figure 2) for comparison with the transient surface displacement observations. For all models, the coseismic rupture geometry consists of a single planar dislocation with strike of 330°, dip of 30°, and length of 96 km, consistent with the seismic focal mechanism and other coseismic models [*Avouac et al*., 2006; *Parsons et al*., 2006; *Pathier et al*., 2006; *Bendick et al*., 2007; *Yan et al*., 2013]. We impose a smoothed slip distribution along the rupture plane, based on averaging the reported coseismic slip distributions from *Avouac et al*. [2006], *Pathier et al*. [2006], and *Yan et al*. [2013]. This coseismic model is smoother than any of the more complicated slip models inverted from interferometric synthetic aperture radar (InSAR), all of which have a more compact region of higher slip and then tails of lower slip. However, published slip models differ in the location and area of the high slip patch. Figure S2 shows maps of total postseismic displacement for specific published slip distributions in a laterally heterogeneous domain. The amount and placement of high slip on the dislocation changes the magnitude of the postseismic displacement, but the spatial pattern including a lobe of relatively large displacements north of the geologic suture does not change with changes to the coseismic slip.

The homogeneous family of models solves for surface displacements due to this dislocation in an elastic-over-viscoelastic layered material, where neither the elastic nor the viscoelastic material varies laterally, although the elastic layer thickness, elastic moduli, and viscosity do vary between versions of the homogeneous model. The viscoelastic layer extends to 100 km, with a free basal boundary condition. Figure S1 shows a comparison between the free basal condition and a symmetry condition, approximating a viscoelastic half-space. Three different families of heterogeneous models all allow differences both in layer thicknesses and in material properties between a northern domain and a southern domain but treat the dislocation interface differently. Locked heterogeneous models fix the dislocation boundaries after rupture, free-slip models allow afterslip over the entire dislocation in any direction, driven by the time-dependent state of stress in the model domain including the rupture zone, and mixed models lock the elastic upper layer but allow free slip on the dislocation within the viscoelastic lower layer. In the two families of models

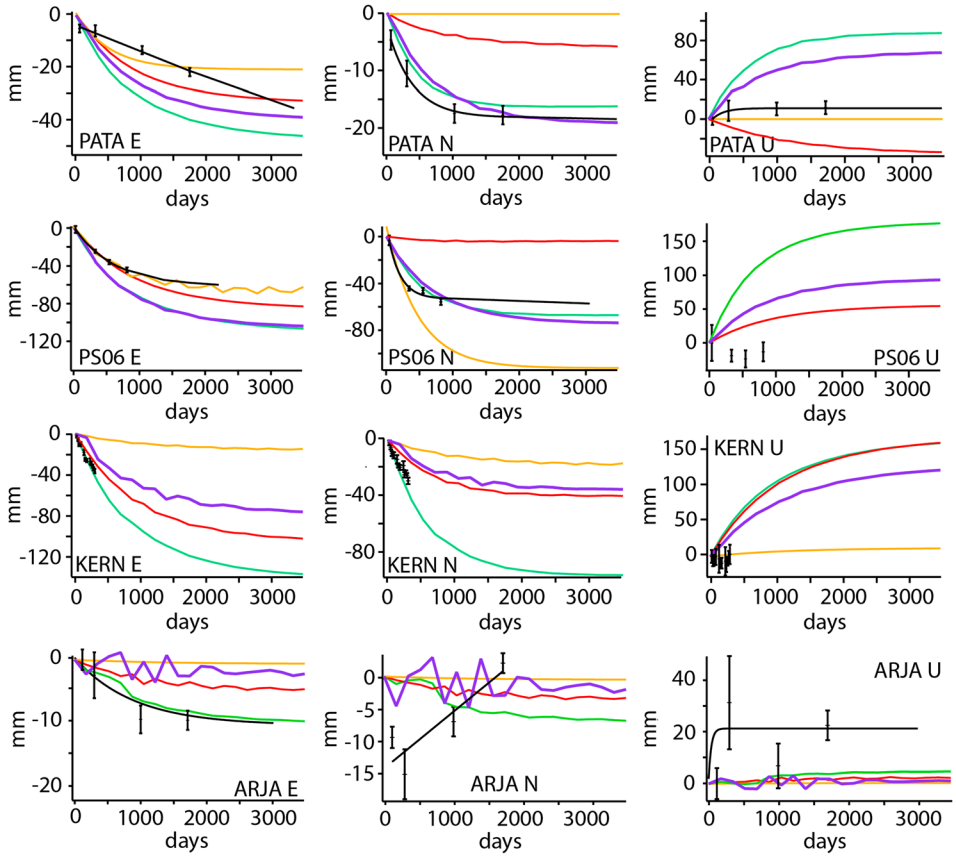

Figure 3. Example time series of modeled and observed surface displacements. PATA, PS19, and KERN are class 1 sites, where the observed time series is within the range of modeled solutions; ARJA is an example of a class 3 site, where the observed series differs in sign or magnitude in at least two components. Class 2 sites differ in sign or magnitude in one component. PATA is located in the northern model domain, PS19 is on the hanging wall of the thrust near the rupture trace, KERN is on the hanging wall far from the trace, and ARJA is on the footwall, all in the southern domain. Colors identify models: black are the observed displacements and fits, purple is the preferred model, green the low competence heterogeneous end-member, orange a representative no afterslip model, and red the best homogeneous model. See Table 1 for model parameters. Figure S3 shows similar plots for all sites used in this study.

that allow afterslip on the dislocation plane and its deeper extension, we do not specify an afterslip function or invert for a slip distribution. Rather, we allow the unlocked part of the dislocation to slip freely in response to the time-dependent state of stress in the model volume. We do not consider poroelastic rebound, which *Wang et al.* [2012] found to be inconsistent with postseismic surface displacements.

We then extract the displacement time series for each location on the model surface corresponding to the GPS observation sites. We use the total displacement at 7 years of elapsed model time for comparison with the observation vectors, and we also plot the observed and simulated time series of displacements for each component of motion (east, north, and up) and classify sites according to the relationship between the observed and simulated series (Figure S3). For some sites with very limited data, the extrapolation of total displacement to 7 years introduces large amounts of uncertainty or is unreasonable. In these cases, we simply score the site according to a comparison of observed and simulated displacements but do not plot a total displacement vector (e.g., PS17 in Figure 4).

Sites are considered class 1 if the observed displacement (including a 2 sigma uncertainty) time series falls within the range of the simulated time series for at least the two horizontal components. Sites are considered class 2 if the observed series is between the numerical solutions for one horizontal component and the other horizontal component has at least the same sign, but the total displacement is either larger or smaller than the time series of simulated displacements. Sites are considered class 3 if the observed horizontal time series are inconsistent with the simulated series. Figure 3 shows

Table 1. Model Setup for Representative Numerical Simulations Shown in Figures[a]

Model Name	South Domain te	North Domain te	South Domain eta	North Domain eta	Other
Best homogeneous	25 km	25 km	1 e 18 Pa s	1 e 18 Pa s	
No afterslip	25 km	5 km	1 e 18 Pa s	7 e 17 Pa s	no afterslip on fault plane
Low competence	20 km	5 km	1 e 18 Pa s	5 e 17 Pa s	
Preferred	25 km	5 km	1 e 18 Pa s	7 e 17 Pa s	

[a]Model families include these specific cases among a wider range of material and geometric parameters. The thickness of the elastic lid is te, and eta is the effective viscosity of the viscous layer.

examples of class 1 and class 3 time series. Finally, we use the classification to score model families, so that the greater the number of class 1 sites, the higher the rank of the associated family of simulations. We use this scoring method to avoid overinterpreting the sparse and discontinuous GPS time series (Figure S3) and score whole families of models with variable geometries and viscosities as a set, rather than individually. This approach means that we develop a preferred family of models based on qualitative characteristics (i.e., homogeneous, heterogeneous, free afterslip, and deep afterslip), rather than a single preferred model of the region.

3. Results

Both the amplitude and the time constant of horizontal displacements in the Kashmir region vary strongly in space. The largest displacements observed with GPS occur in the hanging wall region, consistent with synthetic aperture radar observations from a shorter time span [*Wang and Fialko*, 2014] and with a subset of the GPS sites used here [*Jouanne et al*., 2011]. As in the other studies, our results also demonstrate that the spatial distribution of postseismic deformation is strongly asymmetrical in the strike direction, with GPS sites north of the northern end of the main rupture dislocation having larger displacements than expected for postseismic deformation about a planar dip-slip dislocation [e.g., *Pollitz*, 1997]. In simulations of the postseismic interval, such asymmetry can only be generated by introducing lateral mechanical variations and deep afterslip but is robust for a range of coseismic slip distributions.

Our classification ranking of the consistency of observed with simulated surface displacements therefore allows us to rule out a laterally homogeneous end-member for the westernmost Himalaya, because the family of homogeneous models cannot reproduce large postseismic displacements north of the crustal sutures. Indeed, no homogeneous viscoelastic model fits even the sign of the displacements for sites throughout the extended epicentral region, much less their magnitude, including laterally homogenous models with afterslip at depth. Furthermore, for the homogeneous case, the spatial pattern of class 1 and class 3 sites is systematic, such that individual homogeneous models can be found that fit sites either south of the suture or north of the suture but not both.

Heterogeneous models either with a fully locked or fully free-slipping fault plane outperform homogenous models with respect to the signs of horizontal displacement throughout the epicentral region. However, the solutions with a locked fault plane have surface displacements that are everywhere smaller than the observations. Solutions where the fault plane is allowed to slip all the way to the surface have surface displacements that are almost everywhere too large.

Our preferred model family (Figure 4) includes lateral differences in the thickness of the elastic lid and the viscosity of the viscoelastic layer beneath. It also includes free afterslip on the portion of the fault dislocation in the viscoelastic layer, but the portion of the fault in the elastic lid is locked. We cannot find a single model that fits every observed time series best, but for most sites, the horizontal displacement series are bracketed by simulations with a narrow range of thicknesses and viscosities. Specifically, models with a range of lid thicknesses from 5 to 10 km and viscosities of 1×10^{17} to 1×10^{18} Pa s in the north and lid thicknesses from 20 to 30 km and viscosities from 1×10^{18} to 1×10^{19} Pa s in the south all fit the observations with similar scores, reiterating the well-known tradeoff between elastic thickness and viscosity. The very shallow brittle-ductile transition in the northern domain is consistent with observations of high geothermal gradients in the area, especially around Nanga Parbat [*Meltzer et al*., 2001]. Each model within these ranges is consistent with different subsets

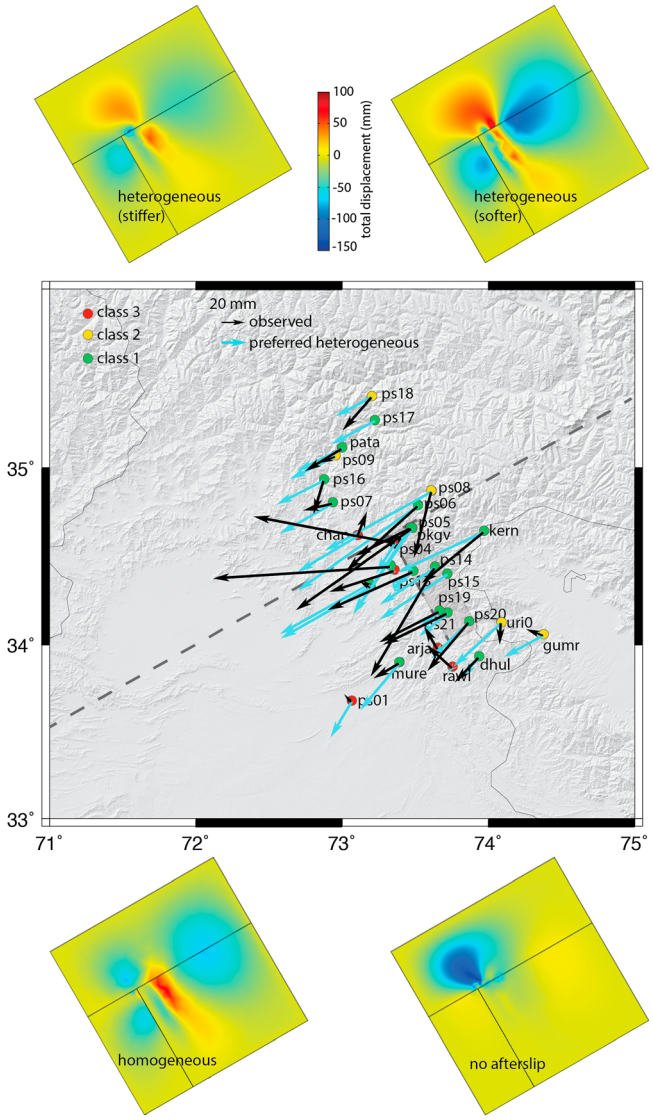

Figure 4. (main) Comparisons of modeled (cyan) to observed (black) total horizontal displacement 7 years after the Kashmir earthquake. The observed vectors are calculated by extrapolating a log fit to the GPS east and north time series to a common epoch, and the model vectors are taken directly from the simulated time series. Grey rectangle shows the model rupture plane, and the dashed lines show the surface trace of the rupture and the simplified suture, for comparison to the maps of simulated total surface displacement. Circle color corresponds to consistency class for our preferred model: class 1 sites (green) are those in which the observed displacement time series plots within the simulated series for both horizontal components; class 2 sites (yellow) are those in which one horizontal component time series plots within the range of simulated series, but the other horizontal component differs in amplitude from the simulated series; class 3 sites (red) are those in which neither horizontal observed series agrees with the simulated series in amplitude or sign. Examples of class 1 and class 3 site time series are shown in Figure 3. (Insets, clockwise from top left) Total surface displacement (**u** + **v** + **w**) for the whole model run of 10 years from the main rupture for the heterogeneous stiff end-member, the heterogeneous soft end-member, the best homogeneous model, and a heterogeneous model with no afterslip.

of sites, with no systematic spatial pattern, suggesting that misfits are likely to be related to smaller-scale mechanical heterogeneity or structural complexity, rather than the quality of observations at particular sites. The most systematic pattern of misfit occurs very near the surface rupture in the footwall, where most sites are misfit by all of the simulations suggesting that the simulations do not capture near-field effects well. Overall, the comparison of observed and simulated displacements requires that crystalline granites and ultramafic rocks of the Kohistan arc have a thinner elastic lid and lower crustal viscosity than the Indian craton with overlying Siwalik sediment to the south.

4. Discussion

Although both the spatial and temporal distribution of displacement observations used in this work are sparse, they suffice to preclude a laterally homogeneous distribution of material properties in the Pakistan Himalaya. Because the crustal-scale faults and sutures present in the epicentral region extend through the entire Himalayan range, this conclusion probably also applies throughout the range. Interseismic observations of shortening across the Himalaya do not require lateral variations in the crustal architecture, confirming the original insight of *Hetland and Hager* [2004] that as the surface velocity field approaches a steady state equilibrium, mechanical differences no longer contribute, especially if they are relatively small. This allows the Himalayan strain field to be approximated as a dislocation in an elastic half-space at interseismic time scales.

The Kashmir heterogeneity of a factor of 5 difference in elastic thickness of the uppermost crust and a factor of 10 difference in lower crustal viscosity probably represents typical intraorogen lithologic contrasts, as the study region contains a primary suture between dominantly sedimentary + felsic crust and dominantly crystalline + mafic crust, but does not express any obvious differences in topographic characteristics or steady state deformation across the suture. In other areas where lateral mechanical heterogeneity has been quantified using postseismic deformation, such as Sichuan [*Huang et al*., 2014] and Sumatra [*Pollitz et al*., 2008], the measured mechanical differences are also expressed in the topography, strain rate, and other proxies such as seismic velocities and are larger than those in Kashmir.

There are some clear limitations to both the modeling and data presented in this work. Several of the sites have very short time series and thus constrain only the immediate postseismic interval. Furthermore, not all of the observed displacement series can be fit with a simple logarithmic function, because of their duration, the number of observation epochs, or the presence of additional terms in the time series beside the expected linear and logarithmic ones (Figure S3). This is why we use consistency scoring rather than strict RMS misfit to evaluate model quality. Of course, the limitations of the scoring mean that we provide only limited constraints on the crustal properties, ruling out strict homogeneity and fault locking, but not producing a unique solution for the fault behavior or crustal architecture.

Our preferred family of models consists of a set of related solutions, each of which fits some subset of the observations better than others. We assume that this is a consequence of three different simplifications in our model development: (1) we ignore local effects, (2) we simplify the contorted MBT and MMT into a planar material discontinuity, and (3) we omit the possibility of surface displacements from a more complex distribution of afterslip, slip on ancillary fault planes, especially north of the MBT/MMT, or from the strongly asymmetrical aftershock distribution. Since even our highly simplified model is already underconstrained, adding these additional complexities is unlikely to give us a better understanding of the basic mechanics.

Finally, because the primary observation requiring lateral heterogeneity is the lobe of large postseismic displacements north of the geologic suture, other mechanisms for producing those surface displacements are possible. For example, *Wang and Fialko* [2014] use a spatially and temporally varying afterslip distribution, and *Jouanne et al*. [2011] propose aseismic slip on a secondary deep dislocation in the north.

5. Conclusions

Postseismic deformation following the Kashmir 2005 earthquake perturbed the interseismic deformation field in the western syntaxis of the Himalaya at a rate that decayed in the 100 km surrounding the earthquake with a time constant of 1–4 years. The amplitude of this postseismic deformation fell to rates close to noise levels in the data (±1 mm/yr) after ~5 years, typical of postseismic deformation elsewhere [e.g., *Wang and Fialko*, 2014; *Bürgmann and Dresen*, 2008; *Huang et al*., 2014; *Pollitz et al*., 2008]. Both the time constants and amplitudes of postseismic displacement vary in space. As a result, and despite limitations imposed by data quality, this study demonstrates that lateral crustal heterogeneity does exist within a continental orogen, that this heterogeneity influences the mechanics of the region, and that some constraints on the magnitude of that heterogeneity can be provided by observations of postseismic deformation.

The mechanical architecture of orogens may play an important role in the long-term spatial organization of horizontal strain, topographic relief, and exhumation rates. It is also possible that the heterogeneity we describe may influence seismic hazards, as mechanical properties determine whether tectonic loading is accommodated by the earthquake cycle or other unrecoverable plastic and viscous mechanisms. At present, although the surface geology clearly indicates compositional differences, a range of applications including elastic strain accumulation for seismic hazard [e.g., *Bollinger et al*., 2004; *Drukpa et al*., 2012; *Schiffman et al*., 2013], orogenic continuum mechanics [e.g., *Bendick and Ehlers*, 2014], and even structural interpretations from geodesy [e.g., *Jouanne et al*., 2011; *Bendick et al*., 2007] all approximate Himalayan architecture as laterally homogeneous. Our data confirm *Hetland and Hager*'s [2004] observation that interpretations of interseismic deformation are less sensitive to this lateral inhomogeneity than measurements of postseismic deformation. This presents an observational challenge that is yet to be addressed. Given the distribution of existing and new GPS stations and the availability of high-quality InSAR data, the postseismic deformation from the recent Nepal earthquakes should reveal much improved constraints on the rheologic architecture of the central Himalaya and southern Tibet.

Acknowledgments
Geodetic observations used in this study are available either through the UNAVCO data archive (RINEX) or by request to the corresponding author for sites observed by non-U.S. researchers (SINEX only).

The Editor thanks Eric Hetland and an anonymous reviewer for their assistance in evaluating this paper.

References

Avouac, J.-P., F. Ayoub, S. Leprince, O. Konca, and D. Helmberger (2006), The 2005 M_w 7.6 Kashmir earthquake: Sub-pixel correlation of ASTER images and seismic waveform analysis, *Earth Planet. Sci. Lett.*, *249*, 514–528.

Bendick, R., and T. Ehlers (2014), Extreme localized exhumation at syntaxes initiated by subduction geometry, *Geophys. Res. Lett.*, *41*, 5861–5867, doi:10.1002/2014GL061026.

Bendick, R., R. Bilham, M. A. Khan, and S. F. Khan (2007), Slip on an active wedge thrust from geodetic observations of the 8 October 2005 Kashmir earthquake, *Geology*, *35*, 267–270.

Bollinger, L., J. P. Avouac, R. Cattin, and M. Pandey (2004), Stress buildup in the Himalaya, *J. Geophys. Res.*, *109*, B11405, doi:10.1029/2003JB002911.

Bürgmann, R., and G. Dresen (2008), Rheology of the lower crust and upper mantle: Evidence from rock mechanics, geodesy, and field observations, *Annu. Rev. Earth Planet. Sci.*, *36*, 531.

Drukpa, D., P. Pelgay, A. Bhattacharya, P. Vernant, W. Szeliga, and R. Bilham (2012), GPS constraints on Indo-Asian convergence in the Bhutan Himalaya: Segmentation and potential for a $8.2 < M_w < 8.8$ earthquake. HKT meeting, Kathmandu, Nepal November 2012, *J. Nepal Geol. Soc*, *45*, 43–44, Special Issue.

Flesch, L., and R. Bendick (2012), The relationship between surface kinematics and deformation of the whole lithosphere, *Geology*, *40*, 711–714, doi:10.1130/G33269.1.

Flesch, L., W. Holt, P. Silver, M. Stephenson, C. Wang, and W. Chan (2005), Constraining the extent of crust-mantle coupling in central Asia using GPS, geologic, and shear wave splitting data, *Earth Planet. Sci. Lett.*, *238*, 248–268.

Hetland, E., and B. Hager (2004), Relationship of geodetic velocities to velocities in the mantle, *Geophys. Res. Lett.*, *31*, L17604, doi:10.1029/2004GL020691.

Huang, M., R. Bürgmann, and A. Freed (2014), Probing the lithospheric rheology across the eastern margin of the Tibetan Plateau, *Earth Planet. Sci. Lett.*, *396*, 88–96.

Jouanne, F., A. Awan, A. Madji, A. Pecher, M. Latif, A. Kausar, J. Mugnier, I. Khan, and N. Khan (2011), Postseismic deformation in Pakistan after the 8 October 2005 earthquake: Evidence of afterslip along a flat north of the Balakot-Bagh thrust, *J. Geophys. Res.*, *116*, B07401, doi:10.1029/2010JB007903.

Khan, M. A., et al. (2008), Preliminary geodetic constraints on plate boundary deformation on the western edge of the Indian Plate from TriGGNnet, *J. Himalayan Earth Sci.*, *41*, 71–87.

Kundu, B., R. Yadav, B. Bali, S. Chowdhury, and V. Gahalaut (2014), Oblique convergence and slip partitioning in the NW Himalaya: Implications from GPS measurements, *Tectonics*, *33*, 2013–2024, doi:10.1002/2014TC003633.

Lechmann, S., D. May, J. Kaus, and S. Schmalholz (2011), Comparing thin-sheet models with 3-D multilayer models for continental collision, *Geophys. J. Int.*, *187*, 10–33.

Li, H., W. Su, C.-Y. Wang, and Z. Huang (2009), Ambient noise Rayleigh wave tomography in western Sichuan and eastern Tibet, *Earth Planet. Sci. Lett.*, *282*, 201–211.

Meltzer, A., G. Sarker, B. Beaudoin, L. Seeber, and J. Armbruster (2001), Seismic characterization of an active metamorphic massif Nanga Parbat, Pakistan Himalaya, *Geology*, *29*, 651–654.

Parsons, T., R. Yeats, Y. Yagi, and A. Hussain (2006), Static stress change from the 8 October, 2005 $M = 7.6$ Kashmir earthquake, *Geophys. Res. Lett.*, *33*, L06304, doi:10.1029/2005GL025429.

Pathier, E., E. Fielding, T. Wright, R. Walker, B. Parsons, and S. Hensley (2006), Displacement field and slip distribution of the 2005 Kashmir earthquake from SAR imagery, *Geophys. Res. Lett.*, *33*, L20310, doi:10.1029/2006GL027193.

Pollitz, F., P. Banerjee, K. Grijalva, B. Nagarajan, and R. Bürgmann (2008), Effect of 3-D viscoelastic structure on post-seismic relaxation from the 2004 $M = 9.2$ Sumatra earthquake, *Geophys. J. Int.*, *173*, 189–204.

Pollitz, F. F. (1997), Gravitational viscoelastic postseismic relaxation on a layered spherical Earth, *J. Geophys. Res.*, *102*, 17,921–17,941, doi:10.1029/97JB01277.

Royden, L., C. Burchfiel, and R. van der Hilst (2008), The geological evolution of the Tibetan Plateau, *Science*, *321*, 1054–1058.

Ryder, I., R. Bürgmann, and F. Pollitz (2011), Lowe crustal relaxation beneath the Tibetan Plateau and Qaidam Basin following the 2001 Kokoxili earthquake, *Geophys. J. Int.*, *187*, 613–630.

Savage, J. (2000), Viscoelastic coupling model for the earthquake cycle driven from below, *J. Geophys. Res.*, *105*, 25,525–25,532, doi:10.1029/2000JB900276.

Schiffman, C., B. S. Bali, W. Szeliga, and R. Bilham (2013), Seismic slip deficit in the Kashmir Himalaya from GPS observations, *Geophys. Res. Lett.*, *40*, 5642–5645, doi:10.1002/2013GL057700.

Searle, M., and M. A. Khan (1996), Geological map of North Pakistan and adjacent areas of northern Ladakh and western Tibet: Oxford, Oxford University, scale 1:650,000.

Wang, E., E. Kirby, K. Furlong, M. van Soest, G. Xu, X. Shi, P. Kamp, and K. Hodges (2012), Two-phase growth of high topography in eastern Tibet during the Cenozoic, *Nat. Geosci.*, *5*, 640–645.

Wang, K., and Y. Fialko (2014), Space geodetic observations and models of postseismic deformation due to the 2005 *M*7.6 Kashmir (Pakistan) earthquake, *J. Geophys. Res. Solid Earth*, *119*, 7306–7318, doi:10.1002/2014JB011122.

Yan, Y., V. Pinel, E. Trouve, E. Pathier, J. Perrin, P. Bascou, and F. Jouanne (2013), Coseismic displacement field and slip distribution of the 2005 Kashmir earthquake from SAR amplitude image correlation and differential interferometry, *Geophys. J. Int.*, *193*, 29–46.

Zatman, S. (2000), On steady rate coupling between an elastic upper crust and a viscous interior, *Geophys. Res. Lett.*, *27*, 2421–2424, doi:10.1029/2000GL011592.